

Electrons herald non-classical light

Germaine Arend,^{1,2,*} Guanhao Huang,^{3,4,*} Armin Feist,^{1,2,†} Yujia Yang,^{3,4,‡}
Jan-Wilke Henke,^{1,2} Zheru Qiu,^{3,4} Hao Jeng,^{1,2} Arslan Sajid Raja,^{3,4} Rudolf
Haindl,^{1,2} Rui Ning Wang,^{3,4} Tobias J. Kippenberg,^{3,4,§} and Claus Ropers^{1,2,¶}

¹Max Planck Institute for Multidisciplinary Sciences, D-37077 Göttingen, Germany

²Georg-August-Universität Göttingen, D-37077 Göttingen, Germany

³Swiss Federal Institute of Technology Lausanne (EPFL), CH-1015 Lausanne, Switzerland

⁴Center for Quantum Science and Engineering, EPFL, Lausanne, Switzerland

ABSTRACT

Free electrons are a widespread and universal source of electromagnetic fields. The past decades witnessed ever-growing control over many aspects of electron-generated radiation, from the incoherent emission produced by X-ray tubes to the exceptional brilliance of free-electron lasers. Reduced to the elementary process of quantized energy exchange between individual electrons and the electromagnetic field, electron beams may facilitate future sources of tunable quantum light. However, the quantum features of such radiation are tied to the correlation of the particles, calling for the joint electronic and photonic state to be explored for further applications. Here, we demonstrate the coherent parametric generation of non-classical states of light by free electrons. We show that the quantized electron energy loss heralds the number of photons generated in a dielectric waveguide. In Hanbury-Brown-Twiss measurements, an electron-heralded single-photon state is revealed via antibunching intensity correlations, while two-quantum energy losses of individual electrons yield pronounced two-photon coincidences. The approach facilitates the tailored preparation of higher-number Fock and other optical quantum states based on controlled interactions with free-electron beams.

One sentence summary: We demonstrate free-electron generated non-classical multiphoton states in a photonic waveguide, leveraging two- and three-particle correlations produced by quantized parametric electron-photon scattering.

Quantum states of light facilitate manifold applications in communication [1], computation [2, 3], and sensing [4, 5]. As a hallmark of quantum optics, photon

number states have no classical counterpart and are essential in quantum metrology [6] and information processing [7, 8]. Furthermore, advanced protocols promise the generation of more exotic states, such as Schrödinger’s cat [9] and GKP states [10] with applications in quantum computing [11–13]. Multiple approaches and platforms have been used for number-state generation, including circuit QED systems [14–16] and superconducting structures [17] in the microwave regime, as well as spontaneous parametric down-conversion [18–22] in the visible to near-infrared.

In the search for new sources of non-classical light, free electrons present an attractive pathway. In pioneering work, electron-excited single quantum emitters, such as color centers and point defects, have already shown antibunching photon statistics in incoherent emission [23–25]. Parametric photon generation by coherent cathodoluminescence [26–32], on the other hand, promises sophisticated photonic states without involving Fermionic excitations, preserves the quantum phase between electrons and photons [33], and allows for enhancements by tunable phase matching [34–36]. In this context, photonic integrated circuits (PICs) [37–39] offer low-loss photon transport, as well as versatile mode tailoring, facilitating efficient scattering between electrons and optical modes [40]. Combining free electrons and PICs thus provides a unique platform for the excitation, control, and observation of classical and quantum optical states at widely variable wavelengths.

A key element of realizing electron-driven quantum light will be to harness the correlations and entanglement of photonic and electronic states. While entanglement remains to be demonstrated, electron-photon coincidence detection [36, 41–46] has yielded detailed information on the joint electron-photon state in time, energy, and momentum. Post-selection of time-correlated electrons and photons was recently shown to improve x-ray elemental mapping [44], as well as photonic-mode imaging and spectroscopy [36, 45]. Furthermore, a temporal fingerprint of the interaction may yield material- and excitation-specific decay times [47, 48] and improve the signal-to-noise ratio (SNR) in electron microscopy [36, 49]. Coherent cathodoluminescence combined with post-selection is further expected to enable the preparation of electron-heralded Fock [50, 51],

* These authors contributed equally.

† armin.feist@mpinat.mpg.de

‡ yujia.yang@epfl.ch

§ tobias.kippenberg@epfl.ch

¶ claus.ropers@mpinat.mpg.de

GKP [11, 52], and other complex quantum states of light [52, 53]. However, the preparation of non-classical optical states via parametric electron-photon interactions has not yet been shown.

Here, we demonstrate the generation of electron-heralded non-classical light using spontaneous parametric scattering in an integrated photonics waveguide. We merge energy-resolved single-electron detection with two-photon coincidence measurements in an optical Hanbury-Brown Twiss (HBT) setup to probe strong correlations between the generated photon number and the quantized electron energy loss. Electron heralding to a single-photon energy change yields prominent photon anti-bunching. The high-contrast detection of threefold coincidences evidences two-photon generation, establishing a novel platform for heralded photon Fock states in integrated photonics-based quantum technology.

In our study, electron-induced photon generation takes place at a Si_3N_4 waveguide ($\sim 80\text{-}\mu\text{m}$ length, $2.2\text{ }\mu\text{m} \times 780\text{ nm}$ cross-section, embedded in SiO_2) on a photonic chip, which is inserted into the sample plane of a transmission electron microscope (TEM) (cf. Fig. 1a). A weakly focused continuous electron beam (100 keV energy, 30 nm beam diameter, 1.1 mrad half angle) passes the waveguide parallel to its surface at an impact parameter (distance to the surface), of about 250 nm (cf. Fig. 1b). Mediated by the structure's dielectric response, the electrons at initial energy E_0 interact with the optical vacuum of the waveguide modes. The interaction generates photons in the modes in a parametric process [36, 43, 54], characterized by a direct energy exchange between electrons and photons that leaves the dielectric material unexcited. The interaction can, thus, be described as an inelastic electron-photon scattering which entangles the final electron energy $E_0 - \sum_{i=1}^k \hbar\omega_i$ with a number of k generated photons at frequencies ω_i . The frequencies generally lie within a spectral continuum of possible excitations (scattering operator given in the SI) [55], defined by phase-matching between the electron (group) velocity and photon phase velocity [34].

In an effective single-mode description, the resulting electron-photon state can be simplified to

$$|\psi_e, \psi_{ph}\rangle = \sum_k c_k |E_0 - k\hbar\omega_0, k\rangle, \quad (1)$$

Here, the coefficients

$$c_k \approx e^{-|g_0|^2/2} g_0^k / \sqrt{k!}, \quad (2)$$

correspond to a Poissonian process of k quantized energy exchanges producing photons near a central optical frequency ω_0 , with a dimensionless coupling constant

$g_0 = \sqrt{\int d\omega |g_\omega|^2}$ obtained by integration over the spectral coupling strength density g_ω .

In the experiment, electrons at 100 keV kinetic energy

pass a straight waveguide. For the given waveguide dimensions, the interaction is dominated by the quasi-TM₀₀ (transverse-magnetic) mode at wavelengths between 1300 and 1400 nm (see simulation results in Fig. 1c). Efficient electron-photon interaction requires a stable lateral positioning of the electron beam inside the evanescent tail of the mode in vacuum. To minimize charging-induced beam deflection, the conductivity of the waveguide surface is enhanced by coating the chip surface with an Indium Tin Oxide (ITO) layer (thickness $< 20\text{ nm}$) (cf. Fig. 1d).

The induced optical state is analyzed by coincidence detection of the generating electrons and the created photons (cf. Fig. 1b). While the photons are guided through fibers to optical single-particle detectors, the electrons are dispersed in a magnetic spectrometer and recorded with an event-based detector (Timepix3 ASIC), which delivers the kinetic energy and arrival time of each electron. The readout electronics of the electron camera further provide time stamps for the arrival time on both photon detectors for electron-photon-photon temporal correlations. We expect to detect different photon numbers k in each parametric electron scattering event, with the k photons being temporally linked to electron energy shifts of $m\hbar\omega_0$ (cf. Fig. 1e). For an ideal electron-photon state (Eq. 1), the photon number and quanta of electron energy change are identical ($k = m$), with probabilities following a Poissonian distribution c_k^2 . In this case, combining temporal particle correlation and electron energy analysis enables heralding schemes, in which the detection of an electron in a specific energy state $|E_0 - k\hbar\omega\rangle$ unambiguously heralds the photon number state $|k\rangle$. In practice, finite optical transmission and inelastic scattering that does not inject light into the waveguide will render the quantized electron energy loss m an upper bound $k \leq m$, which to reach will be a technological target.

We gain access to single- and two-photon generation events and characterize the optical state via an electron-heralded optical HBT detection setup shown in Figures 1a and 2a. Two single-photon detectors A and B placed behind a 50/50 beam splitter are synchronously time-stamped by the electron detector, and every electron is assigned to the closest photon on either detectors, calculating the time delay between them. The analysis of the resulting electron-photon-photon correlation counts $N_{e,A,B}$ is conducted as a function of the electron-energy loss E_{el} and the relative time delays $\tau_A = t_A - t_{el}$ and $\tau_B = t_B - t_{el}$ between the electron and photon detection (arrival times t_{el} , t_A and t_B). An event histogram over these degrees of freedom results in a data cube, which we investigate along cuts or in projection on different axes (cf. Fig. 2b).

The electron-photon correlation as a function of τ_A and E_{el} is given in Fig. 2c. The correlation exhibits a strong coincidence peak separated from the uncor-

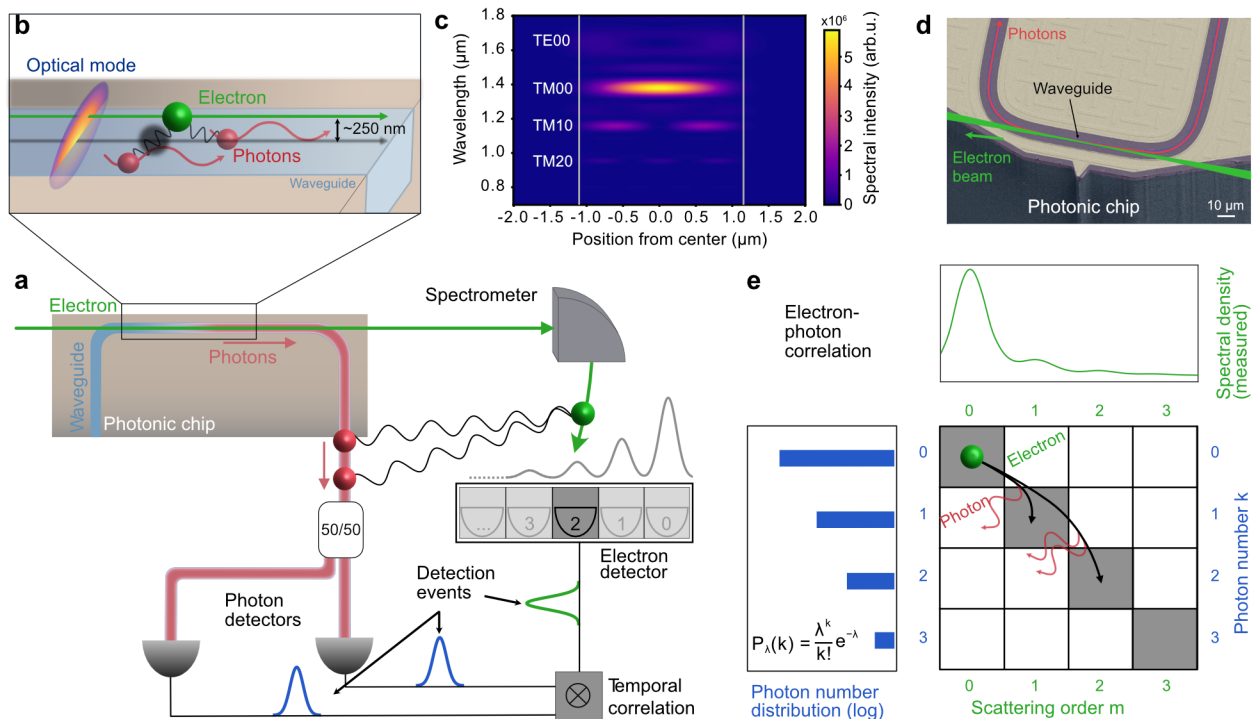


Figure 1. Correlation measurement of waveguide-coupled photons and free electrons. **a** A beam of electrons passes a dielectric waveguide, generating photons that are guided and detected in a fiber-based HBT setup. The electron and photon arrival times are temporally correlated. **b** Enlarged sketch of the interaction region: The electron passes the waveguide surface at an impact parameter of around 250 nm to interact with the evanescent vacuum field of the waveguide modes. **c** Simulation of the photon spectral distribution generated in a 80 μm straight waveguide by 100-keV electrons (impact parameter 250 nm). Gray vertical lines: waveguide boundaries. **d** False-color image of an example photonic chip (scanning electron micrograph). The chip surface is covered with ITO (brighter surface: ITO on metal, darker surface: ITO on Si_3N_4 or on SiO_2 , side walls: SiO_2). **e** Schematic of the correlated quantized electron energy loss and photon number. The electron (green) scatters at the optical mode, generating a random number of photons (red). After detection, the signal correlation links the photon number k (vertical, blue) to the electron scattering order m (horizontal, green). The generation process is expected to follow a Poissonian distribution.

related, mostly unscattered electrons by approximately 0.9 eV (corresponding to a free-space photon wavelength of $\lambda = 1350 - 1420$ nm). Coincidences are found within a temporal interval of 2.9 ns (FWHM, full-width at half-maximum), mainly defined by the electron detection jitter δt_{el} [36]. Above a constant background in τ_A , the temporally confined coincidence peak consists of events in which at least one electron-induced photon was generated, and both a photon and its generating electron were detected. Generally, direct detection of higher photon numbers is possible by employing photon-number resolving detectors [56–59]. The detected electron-photon coincidences primarily originate from the excitation of the detectable TM_{00} mode. Higher-order modes are suppressed in the chip-fiber coupling, and the weakly-excited TE_{00} mode is further diminished due to the detector cut-off wavelength.

Electron-heralded two-photon generation can be observed via a photon A - photon B correlation trace, filtered to true coincidences between photon detector A and

an electron (see Methods). The arising two-dimensional coincidence histogram in Figure 2d is dominated by two photons correlated to electrons with about 1.8 eV = $2\hbar\omega$ energy loss. The photon-photon coincidence peak has a width of 400 ps (FWHM, $\delta t_{\text{ph}} < 300$ ps photon detector jitter). Residual coincidence events in the zero-loss region and the first loss sideband stem from false coincidences due to both electron and photon loss. These false coincidences are also discussed in Figure 4a.

The inelastic electron scattering at the sample is visualized in the electron energy spectra displayed in Figure 3. The uncorrelated spectrum (c.f. Fig. 3a) contains all channels of inelastic electron scattering [60], including material-specific radiative and non-radiative effects, quasi-particle excitation [61] as well as the desired coherent photon generation into optical modes. While the electron energy-loss resulting from electron scattering at a dielectric material can be described by a continuous exponential decay in energy [54], phase-matched parametric photon generation leads to the formation of discrete

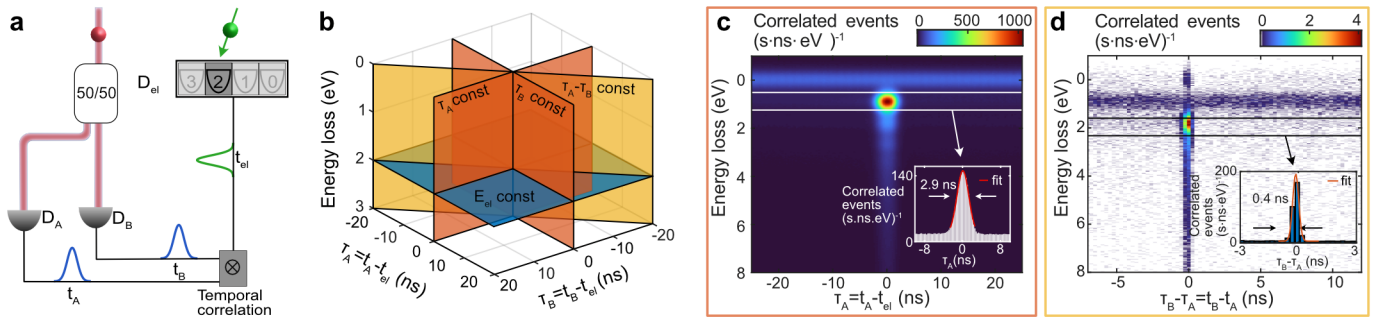


Figure 2. **Three-particle correlation for one electron and two photons.** **a** Schematic of the detection setup with the particle arrival times t_{el} , t_A , t_B on the fiber-coupled photon detectors D_A , D_B and the electron detector D_{el} and electron energy E_{el} as measured parameters. The arrival times are correlated with each other. **b** Parameter space for threefold events. The data is analyzed through lineouts and integrals along different axes. **c** Histogram of electron-photon-photon coincidence events $N_{e,A,B}$ as a function of τ_A and E_{el} , summed over τ_B . Electron-photon scattering causes a coincidence peak at an electron energy shifted downward by around 0.9 eV. Inset: The temporal coincidence uncertainty of around 2.9 ns FWHM represents the timing precision of electron detection. **d** Histogram of particle triples as a function of time delay $t_A - t_B$ and electron energy E_{el} filtered to true coincidences between a photon A and an electron. The coincidences are dominated by electrons that generated 2 photons. (Lowest count rates $< 0.1 \text{ (s} \cdot \text{ns} \cdot \text{eV)}^{-1}$ are kept in lighter colors for better contrast.) Inset: The reduced timing uncertainty of 0.4 ns FWHM follows from the better time resolution in photon detection.

sidebands, downshifted by multiples m of the generated photon's energy $\hbar\omega$ and following a population distribution described by $P_m = |c_m|^2$ (see Equation 2 with $k = m$ and Fig. 1e). As the electron scattering channels at the material and into the optical modes are independent of each other, the measured electron spectrum can be modeled by a convolution of the spectra resulting from broadband scattering and from coherent cathodoluminescence in guided optical modes (cf. SI and Fig. 3a, red).

The spectral component governing coherent photon generation is given by the yellow curve with a peak-to-peak distance between the sidebands close to 0.9 eV. The coupling constant of the coherent electron-photon interaction g_0^{EELS} can be calculated from the population distribution of the individual sidebands P_m (c.f. Fig. 3a, violet to light blue peaks). This distribution generally only holds for a single excited optical mode and constant interaction strength. However, in the experiment, an averaging of the coupling constant is observed, caused by a broadening of the impact parameter due to a nonzero convergence angle and finite beam-focus diameter (cf. Fig. 3b,c), as well as time-dependent beam shifts. Using the population ratio between the first three sidebands in the electron spectra, we obtain an average coupling constant $\langle g_0^{\text{EELS}} \rangle = 0.32$ with a standard deviation of $\Delta_{g_0^{\text{EELS}}} = 0.24$ (see SI for calculations).

Whereas the unheralded electron spectrum includes all inelastic scattering pathways, access to the properties of the detected optical mode is enabled through electron-photon coincidences. The spectra of electrons in coincidence to one (red) or two (yellow) detected photons (cf. Fig. 3d) closely resemble copies of the uncorrelated spectrum (blue) when normalized to the area under the curve (slight deviations in the shape of the coincidence spectra may occur due to transmission losses on the heralding

photons, see SI). The central wavelength of the TM_{00} mode, which dominates the transmitted photons, defines the relative shift of the spectra, and the phase matching bandwidth of the optical mode with 100-keV electrons of 65 meV, corresponding to 100 nm optical wavelength (cf. Fig. 3e) moderately broadens the distributions towards higher scattering orders.

While the previously calculated coupling constant g_0^{EELS} can include multiple inelastic scattering pathways, and thus may be very large [62], a strong coupling to a single optical mode is highly desirable. The coupling strength g_0 of electrons to the detected TM_{00} mode can be determined via Equation 2, taking into account optical losses (see SI for transmission measurements). The detection probability of one or two photons P_1 and P_2 is deduced from the area of the $m = 1$ and $m = 2$ sidebands in the electron-photon and electron-photon-photon coincidence spectra, respectively. They define the number of single- (two-)photon excitation events in which one (two) photons were detected. The calculated $g_0 > 0.2$ is somewhat lower than the value extracted from the electron spectrum, illustrating the necessity of coincident photon detection for disentangling multiple scattering pathways and, in particular, for isolating coherent photon generation.

Beyond the spectral characterization of heralded and unheralded electronic states, we quantitatively study the electron-photon-photon coincidences and their intensity correlations $g^{(2)}$.

Figure 4 analyzes the relative-time histogram $N_{e,A,B}(\tau_A, \tau_B, E_{el})$, that counts threefold correlations at delays τ_A and τ_B with an electron energy E_{el} . Heralding a photonic state by a specific energy change is achieved by integrating over the corresponding energy windows

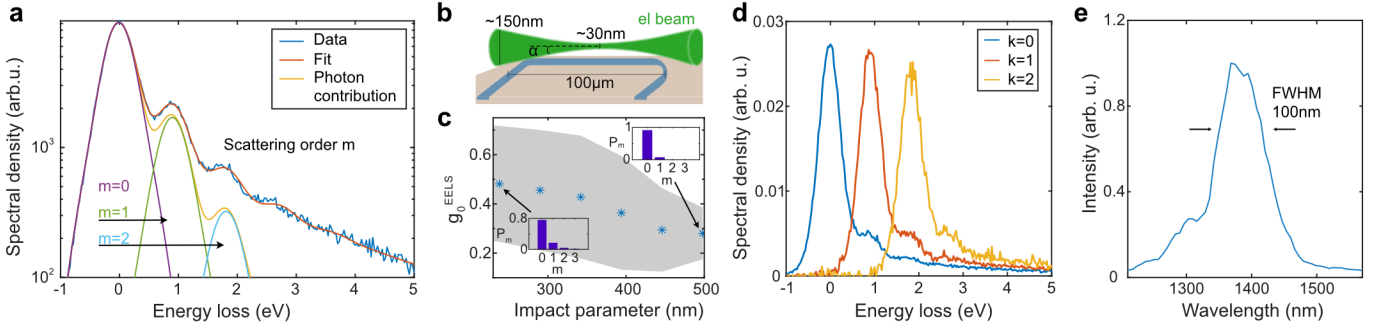


Figure 3. Multiple scattering and heralded electron spectra. **a** Time-averaged (not photon-correlated) electron spectrum (blue), modeled (red) by cascaded m -photon multiple-loss peaks (yellow) and an exponentially decaying continuum. **b** Sketch of the electron-beam caustic traversing the waveguide with a convergence half-angle of $\alpha = 1.1$ mrad, causing some spatial averaging of the coupling constant. **c** Experimentally observed decay of the mean coupling strength towards larger impact parameters (distance to the waveguide). The standard deviation is given as a gray background. The peak height distributions at different g_0^{EELS} are included as insets. **d** Energy distributions of uncorrelated (blue) and correlated electrons (red, yellow) for k detected photons (normalized to the area under the curves). The correlated spectra are obtained by summing over the background-subtracted coincidence peaks shown in Figures 2c,d. **e** Measured optical spectrum with a central peak width of about 100 nm, or 65 meV, normalized to the maximum value.

for single ($m = 1$, Fig. 4a) and two-photon energy loss ($m = 2$, Fig. 4b). True coincidences of electrons with one photon detector $N_{e,\text{AUB}}$ (i.e., at detector D_A OR D_B) lead to vertical/horizontal bands at $\tau_i \approx 0$, while photon-photon coincidences $N_{\text{A}\cap\text{B}}$ (excitation of detectors D_A AND D_B) with or without a corresponding electron emerge on the diagonal line along $\tau_A - \tau_B \approx 0$. Threefold coincidences are found at the intersection of both features (for an in-detail analysis, see SI). While $m = 1$ shows electron single-photon coincidences and some photon-photon coincidences not linked to an electron, the plot for $m = 2$ is dominated by two photons in coincidence with a detected electron. As the three-particle coincidences are mainly confined to the $2\hbar\omega$ loss region (cf. Figures 2b, 3d), they demonstrate the generation of two-photon states via parametric electron scattering with a two-photon energy loss. The temporal widths of the coincidence features follow the respective detector jitters (cf. Fig. 2c,d). Photon-photon coincidences on the diagonal line off the center arise from photon-photon coincidences assigned to a different electron than the generating one, which may either have gone undetected or experienced higher loss.

The correlation between the detected electron energy and the generated photon number renders our scheme a versatile heralded photon-number source. The intrinsic heralding efficiency quantifies how the energy-resolved electron detection predicts the number of generated photons $\eta_i^I = N_{i,j}/(N_j \eta_i^d T_i)$ [63]. This is the probability that, given a heralding particle j is detected, the heralded particle i also exists. In this measurement setup, the heralding efficiency is calculated for the case of observing k photons when selecting an energy window around a specific electron energy loss $m = 1, 2$

and vice versa ($\eta_i^d T_i$: transmission losses and detector efficiencies). Using the count rates from Figure 4a, the efficiencies reach $\eta_e^I > 40\%$ for photon-heralded electrons ($m = 1, 2$) and $\eta_{\text{AUB}}^I = 10\%$ and $\eta_{\text{A}\cap\text{B}}^I = 0.3\%$ for electron-heralded single photons and two photons, respectively. Experimentally, $\eta_{\text{A}\cap\text{B}}^I$ and η_{AUB}^I are limited by spectral overlap of the electron-loss peaks (cf. Fig. 3a), which leads to some mixing in the heralding of photon-number states. Further improvements of the heralding efficiency could, thus, include an enhanced energy resolution [64], and a better coupling ideality to the detected mode [55].

The quality of a heralded signal is further characterized by the coincidence-to-accidental ratio $\text{CAR} = \frac{R_{\text{sig}} - R_{\text{acc}}}{R_{\text{acc}}}$ [63], relating the signal R_{sig} and background R_{acc} rates of coincidences in a specific energy loss region m . A CAR of > 30 is measured for single photons in coincidence with an electron at $m = 1$, showing good fidelity in generating heralded single photons. The CAR value for electron-heralded two-photon events reaches > 150 for $m = 2$, confirming that detected two-photon states are generated predominantly by double-loss of single electrons and not by random coincidences of two single-photon generation events.

To test the non-classicality of the radiation process, i.e., whether it is incompatible with classical field theory, we invoke the Cauchy-Schwarz inequality (CSI) [65] $\gamma = \frac{g_{E,\text{AUB}}^{(2)}(\tau)}{g_E^{(2)} g^{(2)}(0)} \leq 1$, assuming a classical radiation process. The inequality (for derivations, see SI) bounds the temporal cross-correlation between the detected electron energy and photon number $g_{E,\text{AUB}}^{(2)}(\tau)$ to the variation of the electron energy loss $g_E^{(2)} = \frac{\langle \Delta E_{el}^2 \rangle}{\langle \Delta E_{el} \rangle^2}$ and the temporal

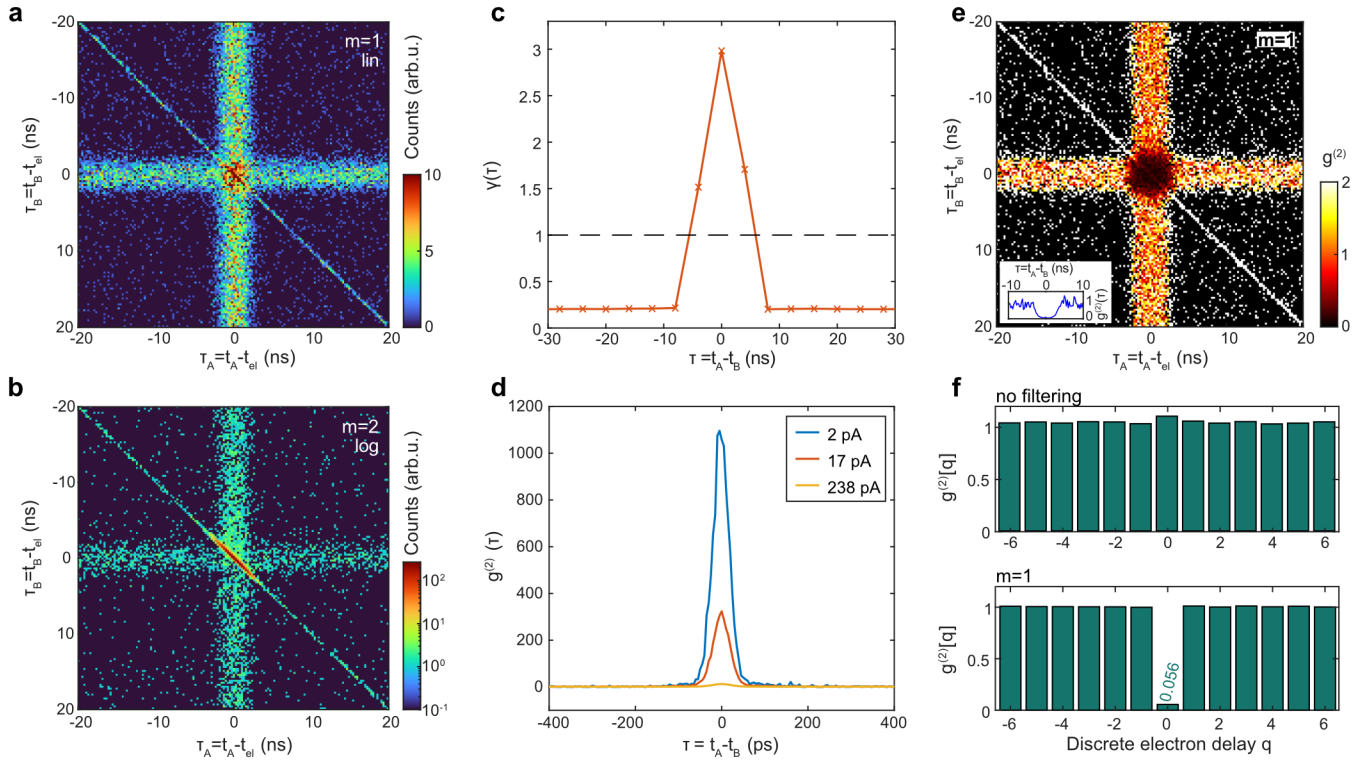


Figure 4. **Statistical analysis of generated photons.** **a,b** Electron-photon-photon correlation events $N_{e,A,B}$ as a function of photon-electron time delays, selected by electron energy: **a** scattering order $m = 1$, and **b** scattering order $m = 2$. **c** Violation of the Cauchy-Schwartz Inequality ($\gamma > 1$) for the electron-photon interaction at different time delays τ (points connected for visibility). **d** Unheralded photon-photon intensity correlation for varying electron current. **e** Electron-heralded photon-photon intensity correlation filtered to the energy region $m = 1$ as a function of both time delays. Inset: Time-averaged $g^{(2)}$ for $m = 1$. **f** Photon-photon intensity correlation as a function of the number of photon-heralding electrons q between the two heralded photons without energy selection (top) and for $m = 1$ (bottom).

intensity correlation of photons in a Hanbury-Brown and Twiss setup $g^{(2)}(\tau)$, normalized to $\tau \gg 0$. For electron-photon coincidence, we find a pronounced violation of the CSI ($\gamma > 1$, cf. Fig. 4c), which proves the non-classical nature of the process [66–68].

This photon statistics of this radiation is further examined by the temporal intensity correlation $g^{(2)}$ of detectors placed in a Hanbury-Brown Twiss (HBT) setup (see Methods). While classical light shows $g^{(2)}(0) \geq g^{(2)}(\tau)$, this is not the case for non-classical light such as single photons or higher photon number states. The unheralded photon-photon intensity correlation (taken with higher time-resolution, higher-efficiency detectors and a time tagger, see Methods) shows a bunching peak at $\tau = 0$ ps [69], inversely proportional to the electron current (cf. Fig. 4d). Following a current-dependent bunching height $g^{(2)}(0) \sim 1/(I\tau_{\text{bin}})$, where I is the electron flux rate and τ_{bin} is the temporal data bin width, this behavior is expected when single electrons can create multiple photons, either in a direct process, as demonstrated here (see SI for further calculations), or as a result of cascaded excitation of multiple two-level

systems leading to incoherent emission [24, 70–72].

The statistics of the electron-heralded photon state are analyzed using the heralded intensity correlation (see Methods)

$$g_H^{(2)}(\tau_A, \tau_B, E_{\text{el}}) = \frac{N_{e,A,B}(\tau_A, \tau_B, E_{\text{el}})}{N_{e,A}(\tau_A, E_{\text{el}})N_{e,B}(\tau_B, E_{\text{el}})} N_e(E_{\text{el}}), \quad (3)$$

relating the occurrence of electron-photon-photon coincidences $N_{e,A,B}$ (cf. Fig. 4a,b) to their single-photon equivalents $N_{e,A/B}$ and the number of heralding electrons N_e . For any energy window E_{el} , $g_H^{(2)}(\tau_A, \tau_B)$ is normalized to single-photon generation ($\tau_{A/B} \approx 0$, $\tau_{B/A} \neq 0$), thus uncovering true threefold coincidences ($\tau_{A \cap B} = 0$).

Figure 4e displays $g_H^{(2)}(\tau_A, \tau_B)$ for single-photon electron-energy losses ($m = 1$), as well as the so-called time-averaged heralded intensity correlation $g_H^{(2)}(\tau)$ reduced to the relative photon delay (inset; see SI for calculation) [73, 74]. The background level and the diagonal feature ($\tau_{A \cap B} \neq 0$) originate from accidental

coincidences (cf. Fig. 4a). For electron-photon-photon coincidences ($\tau_{A \cap B} = 0$), $g_H^{(2)}$ drops sharply to near-zero values, as also visible in the inset. Hence, for $m = 1$, two photons detected at similar times are generated by two different electrons. Usually, accidental and true heralded photon-photon coincidences cannot be distinguished in the heralded intensity correlation if the coherence time is lower than the respective detector jitters [74, 75] (see also SI). However, in our case, the electron-heralded photon-photon coincidences remain distinct due to the much better relative photon detection jitters (see SI). A discrete version of the intensity correlation function $g_H^{(2)}[q]$ substitutes the time delay τ with the number of heralding electrons q between two heralded photons. Here, the detection of two photons from a single electron is compared with random coincidences of two photons heralded by sequential electrons (for details, see Methods). The resulting intensity correlations are shown in Fig. 4f. Without energy filtering (top), a small bunching peak is observed $g_H^{(2)}[0] = 1.10$, similar to the unheralded intensity correlation function (cf. Fig. 4d), but with larger bins corresponding to the electron detector resolution. Filtering to a single-quantum energy exchange ($m = 1$), however, leads to a strong anti-bunching behavior with $g_H^{(2)}(0)$ suppressed to 0.056. The pronounced anti-bunching dip observed for both the time-dependent and discrete intensity correlation functions confirms the high purity of the heralded single-photon state. Two-photon states should, under ideal conditions, also show prominent antibunching. At present, however, technical aspects, including optical losses, electron spectral mixing, and the statistics of the electron source limit the ultimate purity of the heralded state (see SI). Such limitations can be improved upon by time-gated electron sources and enhanced sample designs.

Quantifying our scheme in terms of electron-heralded photon generation requires a separation between different electron scattering pathways. We observe inelastic electron scattering at the material, as well as the parametric photon generation into broadband spatial optical modes. While the electron spectrum shows a mean coupling constant of $g_0^{\text{EELS}} > 0.3$, the scattering into the single detected optical mode features a slightly smaller coupling with $g_0 > 0.2$ (cf. Fig. 3). This is the strongest observed coupling of electrons to a detector-coupled photonic mode observed thus far, facilitated by phase-matched, spatially extended electron-light interaction [34, 36, 76, 77]. Reaching the strong-coupling regime by establishing unity coupling constant to a single optical mode [50, 55, 78–80] will give direct access to a wide class of new phenomena, such as electron-photon entanglement [81–84], photon-induced electron-electron correlations [33, 85] and the generation of more complex non-Gaussian optical states [53].

In conclusion, we introduce electron-heralded quantum states of light, identifying hallmark features such as anti-bunching photon statistics and multiphoton-electron correlations. The scheme will facilitate electron-heralded high-order Fock states, based on further technical optimizations and strong single-mode coupling. Combined with photon or electron state operations, the generation of a wide variety of complex quantum states comes into reach. Broadening the scope of free-electron quantum optics, our results experimentally establish electron beams as a tailored quantum optical resource.

Methods

Fiber-coupled integrated waveguides

The photonic chip with a Si_3N_4 waveguide embedded in SiO_2 is fabricated via the Damascene process [39] onto a Si substrate. The straight part of the waveguide (width \times height $2.2\mu\text{m} \times 780\text{ nm}$) interacting with the electron beam is $80\mu\text{m}$ in length and has no top cladding, allowing for the optical modes to reach into the vacuum and interact with the electron beam. An ITO (indium tin oxide) layer of $< 20\text{ nm}$ thickness (index of refraction $n = 1.99$ at 1550 nm measured at ITO films deposited under similar conditions) on top of the waveguide reduces charging in the presence of an electron beam. The chip is mounted on a custom-made TEM holder [40] such that the waveguide sits in parallel to the electron beam. The optical outputs of the symmetrically-built chip are connected to two short pieces of ultra-high numerical aperture (UHNA-7) fiber, which are spliced to single-mode fibers (SMF-28). The single-mode fibers are sent through the hollowed-out TEM holder and a custom vacuum fiber feedthrough. As the photon generation is directional, the optical detection setup is spliced to the SMF-28 fiber, which is connected to the lower output port.

The main excited optical mode of the waveguide is the quasi- TM_{00} mode due to better phase matching. Further modes are the TE_{00} and higher-order modes. While the TE_{00} mode only shows a small scattering probability in simulations and the phase-matching energy lies in the detection cut-off region, the higher-order waveguide modes are suppressed during their transmission through single-mode optical fibers. Both TM_{00} and TE_{00} show transmission efficiencies around TM_{00} 20%, TE_{00} 25% at the fiber connections. This effectively leads to a spatial single-mode optical detection.

TEM setup

The experiments are conducted at the Göttingen UTEM (JEOL JEM 2100F) with a Schottky field-emission electron source operated in a continuous (thermal-field) mode. The resulting electron beam shows an energy spread of around 0.6 eV at an electron energy of 100 keV . The current is reduced to around 1.4 pA by adjusting the emitter temperature and by using a condenser aperture of $40\mu\text{m}$ diameter to not oversaturate the electron detector. The experiments are conducted in low-magnification STEM (scanning transmission electron microscopy) mode, enabling the positioning and scanning of the focused electron beam (30 nm beam diameter, 1.1 mrad half convergence angle) in the sample plane. The scanning resolution is on the order of 30 nm . All measurements described in the main text are conducted with a stationary electron beam, which is checked and manually readjusted for an optimal combination of photon generation rate and electron transmission onto the detector every 10-30 min. Transmission losses on the electron side arise from charging effects along the waveguide surface, distorting and shifting the electron beam, which reduces incoupling into the 5 mm spectrometer entrance aperture. Post-measurement calculations show an electron transmission efficiency of around 60-70%. For the scanned data, the electron beam is scanned multiple times across the same region (width \times height $200 \times 500\text{ nm}$, 300 ms integration per pixel, pixel size $\sim 40\text{ nm}$). The scanned data is used to measure the position-dependent change of the coupling constant.

Optical setup

The generated photons are sent through the waveguide and optical fibers to the outside of the TEM holder. The fiber end is spliced to a 50/50 beam splitter (Thorlabs TW1550R5A1), which

distributes the photons to two cooled avalanche photodiodes (ID Quantique ID230). As the generated light is measured to be around $1300 - 1400\text{ nm}$, we assume slightly higher losses and a deviation from the 50/50 coupling ratio at the beam splitter. The count rates indicate a splitting ratio of 52/48. The avalanche photodiodes are set to $> 25\%$ detection efficiency and $20\mu\text{s}$ dead time, which leads to 250 and 300 photons/s intrinsic dark counts, respectively, for diode A and B. An evaluation of the transmission and detection efficiency shows an approximate efficiency of detecting a generated photon of 2% per diode. The optical spectrum is measured using a 10 nm flat-top bandpass filter (WL Photonics, tunability from 1200 to 1600 nm), which is set between the TEM holder and the beam splitter, connected to the optical fibers via FC/APC connectors. The transmission band was moved incrementally between 1270 and 1570 nm and the count rate on the detector was measured for every position (see SI). The spectrum shows a central wavelength of 1380 nm and a bandwidth of 100 nm (cf. Fig3e). The unheralded photon-photon intensity correlation is measured with a combination of superconducting nanowire single-photon detectors (Single Quantum) and a time tagger (Swabian Instruments, Time Tagger Ultra). The nanowire detectors show a detection efficiency $> 80\%$ and a time resolution $< 20\text{ ps}$ and, therefore, allow for sharper temporal correlation when operated in combination with a Tagger unit with an RMS jitter of 9 ps .

Event-based electron detector

The electrons are separated in energy via a spectrometer (CEOS GmbH, CEFID) and detected on a hybrid pixel detector based on a Timepix ASID (Amsterdam Scientific Instruments, EM CheeTah T3). Every electron is categorized by its position on the chip (514×514 pixel, 0.03 eV energy bin per pixel) and time-of-arrival (1.56 ns resolution). The stream of data consists of the electron data and the information from both time-to-digital converters at which the photon detector signals arrive. The photon detector signals are time-stamped with a 260 ps bin width and synchronized to the electron time stamps via the same global ASID clock. This allows for temporal correlation of the electron and photon arrival. Further post-acquisition steps are conducted to improve temporal and energy resolution on the electron side: First, a calibration of the individual pixel response times is done with regard to a mean detector response to enhance time resolution [36]. Second, single-particle clustering of the multiple excited pixels with a maximum cluster size of 10 gives access to individual electrons. Their localization follows the arithmetic mean position and the earliest arrival time inside a single cluster. A comparison between external current measurements and event counting on the detector shows an average of 3.4 excited pixels per electron. Last, time-dependent jitters of the electron beam position are reduced on a 10s interval by correcting the position of the zero-loss peak maximum.

For the temporal correlation between electrons and photons, every detected electron is connected to the temporally closest photons on detector A and detector B, and the delay between the arrival times is calculated. The time offset due to propagation delays is measured via the peak position of the electron-photon A, electron-photon B, and photon A-photon B coincidence peaks. These offsets are subtracted for the depicted plots. The connection of electrons with two photons leads to a data set consisting of electron-photon-photon events with electron position on the detector, arrival times of all three particles, as well as time delays between them. For scanned data, the scan position is also included. The electron energy is determined from the position of the zero-loss peak center, which defines the position of 0 eV energy loss, and calibration images of the unscattered electron beam, which give access to the dispersion along the detector.

The electron-photon-photon events can then be analyzed as a

data cube with the axes being the two time delays $\tau_A = t_A - t_{el}$ and $\tau_B = t_B - t_{el}$, as well as the electron energy loss with respect to the uncorrelated zero-loss-peak (ZLP) position. A general fit function (see SI) can describe all features present in the cube. For easier access, individual cuts along or integrals over a specific axis are also analyzed and fitted independently with the fit function defined by the cube fit, as described in the main text.

All data besides the uncorrelated spectrum (Fig. 2) is analysed filtered to a maximum electron-photon time delay of 100 ns, which strongly reduces computation time.

The generation of electron-photon-photon events, combined with large electron currents, can lead to multiple electrons being in coincidence with a single photon. Thus, if multiple electrons are temporarily close to a detected photon, the pair with the smallest time difference is considered a true coincidence, preventing multi-indexing of photons. These true coincidences are used for the analysis of the electron-heralded photon-photon correlation and the discrete intensity correlation.

Intensity correlation

The statistics of photons and the proof for single photon states are often given via the intensity correlation measured in a Hanbury-Brown and Twiss setup: The photons are separated via a 50/50 beam splitter and sent on two photon detectors. Their signal is cross-correlated with each other and normalized to large time delays [63, 86]

$$g^{(2)}(\tau) = \frac{P_{A,B}(\tau)}{P_A P_B}$$

where $P_{A,B}(\tau)$ is the probability of detector A and B being excited at a temporal delay τ to each other, and P_i , $i=A,B$ is the probability of detector excitation A or B. In the given experimental setup, the equation is adjusted for correlation counts N instead of coincidence probabilities $P_i = N_i \tau_b / T_{meas}$ by adding the length of coincidence bins τ_b and the total measurement time T_{meas} .

As the electrons do not arrive uniformly, their statistical arrival distribution plays a role in the unheralded photon-photon intensity correlation. To remove the electron influence, an electron-heralded intensity correlation is employed. Herald intensity correlation follows [73]

$$g^{(2)}(t_A, t_B, t_e) = \frac{P_{A,B,e}(t_A, t_B, t_e) P_e}{P_{A,e}(t_A - t_e) P_{A,e}(t_B - t_e)}$$

in which the photon-photon cross-correlation $P_{A,B,e}(t_A, t_B, t_e)$ is limited to a simultaneous detection of a heralding particle e (see SI for more information). The function is again normalized to large photon-photon time delays, but under the condition that either photon A or photon B is in coincidence with a herald e . For electron-heralding intensity correlation the equation is rewritten in terms of correlation counts N instead of coincidence probabilities, giving rise to Equation 3.

Due to the addition of a third particle, the heralded intensity correlation is a function of two time delays τ_A and τ_B . A reduction to one single variable is done in time-averaged intensity correlation [73, 74]

$$g^{(2)}(\tau_A = 0, \tau = \tau_B) = \frac{P_{A,B,e}(\tau) P_e}{P_{A,e}(0) P_{A,e}(\tau)}$$

in which one time delay τ_A is set to coincidence. Thus, the second photon B is simultaneously cross-correlated with a photon A and an electron. Now two correlation functions $P_{A,B,e}(\tau)$ and $P_{B,e}(\tau)$ define the shape of the curve, both possibly widened by detector jitters.

For a discrete intensity correlation function, two photons are correlated as a function of the number of heralds between their arrival q , comparing the number of successful coincidences between two photons correlated to the same electron ($q = 0$) to the number of successful coincidences of two photons correlated to two different electrons ($q \neq 0$) assuming the electrons came at the same time. A successful coincidence is defined by setting a time interval, given by the temporal jitters of the system, in which two particles have to arrive compared to each other.

The normalization for large q is given by the number of electron-photon coincidences $N_{e,A/e,B}$ and the number of heralding events N_e , giving

$$g^{(2)}[q] = \frac{N_{e,A,B}[q] N_e}{N_{e,A} N_{e,B}} \quad (4)$$

Due to the random arrival times of electrons in the given setup, q can not be directly converted to a time delay, compared to periodic sources such as pulsed single photon sources using the pulse trigger as a herald.

-
- [1] R. Ursin, F. Tiefenbacher, T. Schmitt-Manderbach, H. Weier, T. Scheidl, M. Lindenthal, B. Blauensteiner, T. Jennewein, J. Perdigues, P. Trojek, B. Ömer, M. Fürst, M. Meyenburg, J. Rarity, Z. Sodnik, C. Barbieri, H. Weinfurter, and A. Zeilinger, Entanglement-based quantum communication over 144 km, *Nature Phys* **3**, 481 (2007).
- [2] P. Kok, W. J. Munro, K. Nemoto, T. C. Ralph, J. P. Dowling, and G. J. Milburn, Linear optical quantum computing with photonic qubits, *Rev. Mod. Phys.* **79**, 135 (2007).
- [3] H.-S. Zhong, H. Wang, Y.-H. Deng, M.-C. Chen, L.-C. Peng, Y.-H. Luo, J. Qin, D. Wu, X. Ding, Y. Hu, P. Hu, X.-Y. Yang, W.-J. Zhang, H. Li, Y. Li, X. Jiang, L. Gan, G. Yang, L. You, Z. Wang, L. Li, N.-L. Liu, C.-Y. Lu, and J.-W. Pan, Quantum computational advantage using photons, *Science* **370**, 1460 (2020).
- [4] C. L. Degen, F. Reinhard, and P. Cappellaro, Quantum sensing, *Rev. Mod. Phys.* **89**, 035002 (2017).
- [5] D. Ganapathy, LIGO O4 Detector Collaboration, and et al., Broadband Quantum Enhancement of the LIGO Detectors with Frequency-Dependent Squeezing, *Phys. Rev. X* **13**, 041021 (2023).
- [6] M. J. Holland and K. Burnett, Interferometric detection of optical phase shifts at the Heisenberg limit, *Phys. Rev. Lett.* **71**, 1355 (1993).
- [7] M. A. Broome, A. Fedrizzi, S. Rahimi-Keshari, J. Dove, S. Aaronson, T. C. Ralph, and A. G. White, Photonic Boson Sampling in a Tunable Circuit, *Science* **339**, 794 (2013).
- [8] C. S. Wang, J. C. Curtis, B. J. Lester, Y. Zhang, Y. Y. Gao, J. Freeze, V. S. Batista, P. H. Vaccaro, I. L. Chuang, L. Frunzio, L. Jiang, S. M. Girvin, and R. J. Schoelkopf, Efficient Multiphoton Sampling of Molecular Vibronic Spectra on a Superconducting Bosonic Processor, *Phys. Rev. X* **10**, 021060 (2020).
- [9] A. Ourjoumtsev, H. Jeong, R. Tualle-Brouiri, and P. Grangier, Generation of optical ‘Schrödinger cats’ from

- photon number states, *Nature* **448**, 784 (2007).
- [10] D. Gottesman, A. Kitaev, and J. Preskill, Encoding a qubit in an oscillator, *Phys. Rev. A* **64**, 012310 (2001).
- [11] G. Baranes, S. Even-Haim, R. Ruimy, A. Gorlach, R. Dahan, A. A. Diringer, S. Hacoheh-Gourgy, and I. Kaminer, Free-electron interactions with photonic GKP states: Universal control and quantum error correction, *Phys. Rev. Research* **5**, 043271 (2023).
- [12] P. Campagne-Ibarcq, A. Eickbusch, S. Touzard, E. Zalys-Geller, N. E. Frattini, V. V. Sivak, P. Reinhold, S. Puri, S. Shankar, R. J. Schoelkopf, L. Frunzio, M. Mirrahimi, and M. H. Devoret, Quantum error correction of a qubit encoded in grid states of an oscillator, *Nature* **584**, 368 (2020).
- [13] U. Réglade, A. Bocquet, R. Gautier, J. Cohen, A. Marquet, E. Albertinale, N. Pankratova, M. Hallén, F. Rautschke, L.-A. Sellem, P. Rouchon, A. Sarlette, M. Mirrahimi, P. Campagne-Ibarcq, R. Lescanne, S. Jezouin, and Z. Leghtas, Quantum control of a cat qubit with bit-flip times exceeding ten seconds, *Nature* **629**, 778 (2024).
- [14] J. Geremia, Deterministic and Nondestructively Verifiable Preparation of Photon Number States, *Phys. Rev. Lett.* **97**, 073601 (2006).
- [15] X. Zhou, I. Dotsenko, B. Peaudcerf, T. Rybarczyk, C. Sayrin, S. Gleyzes, J. M. Raimond, M. Brune, and S. Haroche, Field Locked to a Fock State by Quantum Feedback with Single Photon Corrections, *Phys. Rev. Lett.* **108**, 243602 (2012).
- [16] M. Uria, P. Solano, and C. Hermann-Avigliano, Deterministic Generation of Large Fock States, *Phys. Rev. Lett.* **125**, 093603 (2020).
- [17] M. Hofheinz, E. M. Weig, M. Ansmann, R. C. Bialczak, E. Lucero, M. Neeley, A. D. O’Connell, H. Wang, J. M. Martinis, and A. N. Cleland, Generation of Fock states in a superconducting quantum circuit, *Nature* **454**, 310 (2008).
- [18] E. Waks, E. Diamanti, and Y. Yamamoto, Generation of photon number states, *New J. Phys.* **8**, 4 (2006).
- [19] A. Ourjoumtsev, R. Tualle-Brouiri, and P. Grangier, Quantum Homodyne Tomography of a Two-Photon Fock State, *Phys. Rev. Lett.* **96**, 213601 (2006).
- [20] M. Cooper, L. J. Wright, C. Söller, and B. J. Smith, Experimental generation of multi-photon Fock states, *Opt. Express* **21**, 5309 (2013).
- [21] J. Tiedau, T. J. Bartley, G. Harder, A. E. Lita, S. W. Nam, T. Gerrits, and C. Silberhorn, Scalability of parametric down-conversion for generating higher-order Fock states, *Phys. Rev. A* **100**, 041802 (2019).
- [22] G. Harder, T. J. Bartley, A. E. Lita, S. W. Nam, T. Gerrits, and C. Silberhorn, Single-Mode Parametric-Down-Conversion States with 50 Photons as a Source for Mesoscopic Quantum Optics, *Phys. Rev. Lett.* **116**, 143601 (2016).
- [23] R. Bourrellier, S. Meuret, A. Tararan, O. Stéphan, M. Kociak, L. H. G. Tizei, and A. Zobelli, Bright UV Single Photon Emission at Point Defects in h -BN, *Nano Lett.* **16**, 4317 (2016).
- [24] S. Fiedler, S. Morozov, D. Komisar, E. A. Ekimov, L. F. Kulikova, V. A. Davydov, V. N. Agafonov, S. Kumar, C. Wolff, S. I. Bozhevolnyi, and N. A. Mortensen, Sub-to-super-Poissonian photon statistics in cathodoluminescence of color center ensembles in isolated diamond crystals, *Nanophotonics* **12**, 2231 (2023).
- [25] L. H. G. Tizei and M. Kociak, Spatially Resolved Quantum Nano-Optics of Single Photons Using an Electron Microscope, *Phys. Rev. Lett.* **110**, 153604 (2013).
- [26] E. J. R. Vesseur, R. de Waele, M. Kuttge, and A. Polman, Direct Observation of Plasmonic Modes in Au Nanowires Using High-Resolution Cathodoluminescence Spectroscopy, *Nano Lett.* **7**, 2843 (2007).
- [27] J. Christopher, M. Taleb, A. Maity, M. Hentschel, H. Giessen, and N. Talebi, Electron-driven photon sources for correlative electron-photon spectroscopy with electron microscopes, *Nanophotonics* **9**, 4381 (2020).
- [28] B. J. M. Brenny, T. Coenen, and A. Polman, Quantifying coherent and incoherent cathodoluminescence in semiconductors and metals, *Journal of Applied Physics* **115**, 244307 (2014).
- [29] T. Coenen, F. Bernal Arango, A. Femius Koenderink, and A. Polman, Directional emission from a single plasmonic scatterer, *Nat Commun* **5**, 3250 (2014).
- [30] T. Coenen and N. M. Haegel, Cathodoluminescence for the 21st century: Learning more from light, *Applied Physics Reviews* **4**, 031103 (2017).
- [31] T. Sannomiya, A. Konečná, T. Matsukata, Z. Thollar, T. Okamoto, F. J. García de Abajo, and N. Yamamoto, Cathodoluminescence Phase Extraction of the Coupling between Nanoparticles and Surface Plasmon Polaritons, *Nano Lett.* **20**, 592 (2020).
- [32] M. Scheucher, T. Schachinger, T. Spielauer, M. Stöger-Pollach, and P. Haslinger, Discrimination of coherent and incoherent cathodoluminescence using temporal photon correlations, *Ultramicroscopy* **241**, 113594 (2022).
- [33] O. Kfir, V. Di Giulio, F. J. G. de Abajo, and C. Ropers, Optical coherence transfer mediated by free electrons, *Sci. Adv.* **7**, eabf6380 (2021).
- [34] O. Kfir, H. Lourenço-Martins, G. Storeck, M. Sivilis, T. R. Harvey, T. J. Kippenberg, A. Feist, and C. Ropers, Controlling free electrons with optical whispering-gallery modes, *Nature* **582**, 46 (2020).
- [35] N. Müller, V. Hock, H. Koch, N. Bach, C. Rathje, and S. Schäfer, Broadband Coupling of Fast Electrons to High-Q Whispering-Gallery Mode Resonators, *ACS Photonics* **8**, 1569 (2021).
- [36] A. Feist, G. Huang, G. Arend, Y. Yang, J.-W. Henke, A. S. Raja, F. J. Kappert, R. N. Wang, H. Lourenço-Martins, Z. Qiu, J. Liu, O. Kfir, T. J. Kippenberg, and C. Ropers, Cavity-mediated electron-photon pairs, *Science* **377**, 777 (2022).
- [37] J. Wang, F. Sciarrino, A. Laing, and M. G. Thompson, Integrated photonic quantum technologies, *Nat. Photonics* **14**, 273 (2020).
- [38] A. W. Elshaari, W. Pernice, K. Srinivasan, O. Benson, and V. Zwiller, Hybrid integrated quantum photonic circuits, *Nat. Photonics* **14**, 285 (2020).
- [39] J. Liu, G. Huang, R. N. Wang, J. He, A. S. Raja, T. Liu, N. J. Engelsen, and T. J. Kippenberg, High-yield, wafer-scale fabrication of ultralow-loss, dispersion-engineered silicon nitride photonic circuits, *Nature Communications* **12**, 2236 (2021).
- [40] J.-W. Henke, A. S. Raja, A. Feist, G. Huang, G. Arend, Y. Yang, F. J. Kappert, R. N. Wang, M. Möller, J. Pan, J. Liu, O. Kfir, C. Ropers, and T. J. Kippenberg, Integrated photonics enables continuous-beam electron phase modulation, *Nature* **600**, 653 (2021).
- [41] P. Kruit, H. Shuman, and A. Somlyo, Detection of X-rays and electron energy loss events in time coincidence,

- Ultramicroscopy* **13**, 205 (1984).
- [42] R. J. Graham, J. Spence, and H. Alexander, Infrared Cathodoluminescence Studies from Dislocations in Silicon in tem, a Fourier Transform Spectrometer for Cl in Tem and Els/cl Coincidence Measurements of Lifetimes in Semiconductors, *MRS Proc.* **82**, 235 (1986).
- [43] X. Bendaña, A. Polman, and F. J. García de Abajo, Single-Photon Generation by Electron Beams, *Nano Lett.* **11**, 5099 (2011).
- [44] D. Jannis, K. Müller-Caspary, A. Béch e, A. Oelsner, and J. Verbeeck, Spectroscopic coincidence experiments in transmission electron microscopy, *Appl. Phys. Lett.* **114**, 143101 (2019).
- [45] N. Varkentina, Y. Auad, S. Y. Woo, A. Zobelli, L. Bocher, J.-D. Blazit, X. Li, M. Tenc e, K. Watanabe, T. Taniguchi, O. St ephan, M. Kociak, and L. H. G. Tizei, Cathodoluminescence excitation spectroscopy: Nanoscale imaging of excitation pathways, *Sci. Adv.* **8**, eabq4947 (2022).
- [46] S. Yanagimoto, N. Yamamoto, T. Yuge, H. Saito, K. Akiba, and T. Sannomiya, Time-correlated electron and photon counting microscopy, *Commun Phys* **6**, 260 (2023).
- [47] N. Varkentina, Y. Auad, S. Y. Woo, F. Castioni, J.-D. Blazit, M. Tenc e, H.-C. Chang, J. Chen, K. Watanabe, T. Taniguchi, M. Kociak, and L. H. G. Tizei, Excitation lifetime extracted from electron–photon (EELS-CL) nanosecond-scale temporal coincidences, *Applied Physics Letters* **123**, 223502 (2023).
- [48] M. Taleb, P. Bittorf, M. Black, M. Hentschel, W. Sigle, B. Haas, C. Koch, P. van Aken, H. Giessen, and N. Talebi, *Ultrafast phonon-mediated dephasing of color centers in hexagonal boron nitride probed by electron beams* (2024).
- [49] S. A. Koppell, J. W. Simonaitis, M. A. R. Krielaart, W. P. Putnam, K. K. Berggren, and P. D. Keathley, Analysis and Applications of a Heralded Electron Source (2024), [arXiv:2406.18755 \[physics\]](https://arxiv.org/abs/2406.18755).
- [50] O. Kfir, Entanglements of electrons and cavity-photons in the strong coupling regime, *Phys. Rev. Lett.* **123**, 103602 (2019).
- [51] A. Ben Hayun, O. Reinhardt, J. Nemirovsky, A. Karnieli, N. Rivera, and I. Kaminer, Shaping quantum photonic states using free electrons, *Sci. Adv.* **7**, eabe4270 (2021).
- [52] R. Dahan, G. Baranes, A. Gorlach, R. Ruimy, N. Rivera, and I. Kaminer, Creation of Optical Cat and GKP States Using Shaped Free Electrons, *Phys. Rev. X* **13**, 031001 (2023).
- [53] M. Sirotin, A. Rasputnyi, T. Chlouba, R. Shiloh, and P. Hommelhoff, Quantum Optics with Recoiled Free Electrons (2024), [arXiv:2405.06560 \[quant-ph\]](https://arxiv.org/abs/2405.06560).
- [54] F. J. Garc a de Abajo, Optical excitations in electron microscopy, *Reviews of Modern Physics* **82**, 209 (2010).
- [55] G. Huang, N. J. Engelsen, O. Kfir, C. Ropers, and T. J. Kippenberg, Electron-Photon Quantum State Heralding Using Photonic Integrated Circuits, *PRX Quantum* **4**, 020351 (2023).
- [56] F. Marsili, D. Bitauld, A. Gaggero, S. Jahanmirinejad, R. Leoni, F. Mattioli, and A. Fiore, Physics and application of photon number resolving detectors based on superconducting parallel nanowires, *New J. Phys.* **11**, 045022 (2009).
- [57] C. J. Chunnillall, I. P. Degiovanni, S. K uck, I. M uller, and A. G. Sinclair, Metrology of single-photon sources and detectors: A review, *Opt. Eng* **53**, 081910 (2014).
- [58] M. Schmidt, M. von Helversen, M. L opez, F. Gericke, E. Schlottmann, T. Heindel, S. K uck, S. Reitzenstein, and J. Beyer, Photon-Number-Resolving Transition-Edge Sensors for the Metrology of Quantum Light Sources, *J Low Temp Phys* **193**, 1243 (2018).
- [59] M. von Helversen, J. B ohm, M. Schmidt, M. Gschrey, J.-H. Schulze, A. Strittmatter, S. Rodt, J. Beyer, T. Heindel, and S. Reitzenstein, Quantum metrology of solid-state single-photon sources using photon-number-resolving detectors, *New J. Phys.* **21**, 035007 (2019).
- [60] R. F. Egerton, Electron energy-loss spectroscopy in the TEM, *Rep. Prog. Phys.* **72**, 016502 (2009).
- [61] P. Schattschneider, F. F odermayr, and D.-S. Su, Coherent double-plasmon excitation in aluminum, *Phys. Rev. Lett.* **59**, 724 (1987).
- [62] Y. Adiv, H. Hu, S. Tseses, R. Dahan, K. Wang, Y. Kurman, A. Gorlach, H. Chen, X. Lin, G. Bartal, and I. Kaminer, Observation of 2D Cherenkov Radiation, *Phys. Rev. X* **13**, 011002 (2023).
- [63] S. Signorini and L. Pavesi, On-chip heralded single photon sources, *AVS Quantum Sci.* **2**, 041701 (2020).
- [64] Y. Auad, C. Hamon, M. Tenc e, H. Lourenço-Martins, V. Mkhitaryan, O. St ephan, F. J. Garc a de Abajo, L. H. G. Tizei, and M. Kociak, Unveiling the Coupling of Single Metallic Nanoparticles to Whispering-Gallery Microcavities, *Nano Lett.* **22**, 319 (2022).
- [65] M. D. Reid and D. F. Walls, Violations of classical inequalities in quantum optics, *Phys. Rev. A* **34**, 1260 (1986).
- [66] J. F. Clauser, Experimental distinction between the quantum and classical field-theoretic predictions for the photoelectric effect, *Phys. Rev. D* **9**, 853 (1974).
- [67] R. Riedinger, S. Hong, R. A. Norte, J. A. Slater, J. Shang, A. G. Krause, V. Anant, M. Aspelmeyer, and S. Gr oblacher, Non-classical correlations between single photons and phonons from a mechanical oscillator, *Nature* **530**, 313 (2016).
- [68] S. Meesala, S. Wood, D. Lake, P. Chiappina, C. Zhong, A. D. Beyer, M. D. Shaw, L. Jiang, and O. Painter, Non-classical microwave-optical photon pair generation with a chip-scale transducer, *Nat. Phys.* **20**, 871 (2024).
- [69] S. Yanagimoto, N. Yamamoto, T. Yuge, T. Sannomiya, and K. Akiba, *Unveiling the nature of cathodoluminescence from photon statistics* (2024).
- [70] S. Meuret, L. H. G. Tizei, T. Cazimajou, R. Bourrellier, H. C. Chang, F. Treussart, and M. Kociak, Photon Bunching in Cathodoluminescence, *Phys. Rev. Lett.* **114**, 197401 (2015).
- [71] T. Yuge, N. Yamamoto, T. Sannomiya, and K. Akiba, Superbunching in cathodoluminescence: A master equation approach, *Phys. Rev. B* **107**, 165303 (2023).
- [72] M. Sol a-Garcia, K. W. Mauser, M. Liebrau, T. Coenen, S. Christiansen, S. Meuret, and A. Polman, Photon Statistics of Incoherent Cathodoluminescence with Continuous and Pulsed Electron Beams, *ACS Photonics* **8**, 916 (2021).
- [73] E. Bocquillon, C. Couteau, M. Razavi, R. Laflamme, and G. Weihs, Coherence measures for heralded single-photon sources, *Phys. Rev. A* **79**, 035801 (2009).
- [74] S. Bettelli, Comment on “Coherence measures for heralded single-photon sources”, *Phys. Rev. A* **81**, 037801 (2010).
- [75] D. H ockel, L. Koch, and O. Benson, Direct measurement

- of heralded single-photon statistics from a parametric down-conversion source, *Phys. Rev. A* **83**, 013802 (2011).
- [76] R. Dahan, S. Nehemia, M. Shentcis, O. Reinhardt, Y. Adiv, X. Shi, O. Be'er, M. H. Lynch, Y. Kurman, K. Wang, and I. Kaminer, Resonant phase-matching between a light wave and a free-electron wavefunction, *Nature Physics* **16**, 1123 (2020).
- [77] M. Bézard, I. Si Hadj Mohand, L. Ruggiero, A. Le Roux, Y. Auad, P. Baroux, L. H. G. Tizei, X. Checoury, and M. Kociak, High-Efficiency Coupling of Free Electrons to Sub- λ^3 Modal Volume, High-Q Photonic Cavities, *ACS Nano* **18**, 10417 (2024).
- [78] Z. Zhao, Upper bound for the quantum coupling between free electrons and photons (2024), [arXiv:2404.01221](https://arxiv.org/abs/2404.01221) [physics, physics:quant-ph].
- [79] Z. Xie, Z. Chen, H. Li, Q. Yan, H. Chen, X. Lin, I. Kaminer, O. D. Miller, and Y. Yang, Maximal quantum interaction between free electrons and photons (2024), [arXiv:2404.00377](https://arxiv.org/abs/2404.00377) [cond-mat, physics:physics, physics:quant-ph].
- [80] A. Karnieli, C. Roques-Carmes, N. Rivera, and S. Fan, Strong Coupling and Single-Photon Nonlinearity in Free-Electron Quantum Optics, *ACS Photonics*, [acsphotonics.4c00908](https://doi.org/10.1021/acsp Photonics.4c00908) (2024).
- [81] E. Rotunno, S. Gargiulo, G. M. Vanacore, C. Mechel, A. H. Tavabi, R. E. Dunin-Borkowski, F. Carbone, I. Madan, S. Frabboni, T. Guner, E. Karimi, I. Kaminer, and V. Grillo, One-Dimensional “Ghost Imaging” in Electron Microscopy of Inelastically Scattered Electrons, *ACS Photonics*, [acsphotonics.2c01925](https://doi.org/10.1021/acsp Photonics.2c01925) (2023).
- [82] T. P. Rasmussen, Á. R. Echarri, J. D. Cox, and F. J. G. De Abajo, Generation of entangled waveguided photon pairs by free electrons, *Sci. Adv.* **10**, eadn6312 (2024).
- [83] J.-W. Henke, H. Jeng, and C. Ropers, Quantum eraser experiments for the demonstration of entanglement between swift electrons and light (2024), [arXiv:2404.11368](https://arxiv.org/abs/2404.11368) [quant-ph].
- [84] E. Kazakevich, H. Aharon, and O. Kfir, On spatial electron-photon entanglement (2024), [arXiv:2404.18936](https://arxiv.org/abs/2404.18936) [physics.gen-ph].
- [85] S. Kumar, J. Lim, N. Rivera, W. Wong, Y. S. Ang, L. K. Ang, and L. J. Wong, Strongly correlated multielectron bunches from interaction with quantum light, *Sci. Adv.* **10**, eadm9563 (2024).
- [86] A. Migdall, S. Polyakov, J. Fan, and J. Bienfang, eds., *Single-Photon Generation and Detection*, Experimental Methods in the Physical Sciences No. volume 45 (Elsevier/AP, Academic Press is an imprint of Elsevier, Amsterdam ; Boston, 2013).

sterdam ; Boston, 2013).

DATA AVAILABILITY STATEMENT

The code and data used to produce the figures in this work will be published in the repository [Zenodo](https://zenodo.org/) upon publication of the paper.

ACKNOWLEDGEMENTS

We thank the members of the EBEAM consortium, in particular F. J. García de Abajo, Albert Polman, Mathieu Kociak and Saskia Fiedler, for fruitful discussions.

Funding Information: All samples were fabricated in the Center of MicroNanoTechnology (CMi) at EPFL. This material is based upon work supported by the Air Force Office of Scientific Research under award number FA9550-15-1-0250 and was further supported by the Swiss National Science Foundation under grant agreements 185870 (Ambizione), 182103, and 176563 (BRIDGE). All experiments were carried out at the Göttingen UTEM Lab, which was funded by the Max Planck Society, the Deutsche Forschungsgemeinschaft (DFG, German Research Foundation) through 432680300/SFB 1456 (project C01) and the Gottfried Wilhelm Leibniz program, and the European Union’s Horizon 2020 research and innovation program under grant agreement No. 101017720 (FET-Proactive EBEAM). Y.Y. acknowledges support from the EU H2020 research and innovation program under the Marie Skłodowska-Curie IF grant agreement No. 101033593 (SEPhIM).

Author contribution: A.S.R. and Y.Y. designed the photonic chip device. Z.Q. optimized the coating and fabricated the device together with R.N.W.. Y.Y. optically characterized the chip and A.S.R. packaged it. J.W.H. designed the TEM sample mount. G.A. built the optical setup and performed the TEM experiments. A.F. implemented the clustering and time-tagging of the event-based data, supported by R.H.. The data was analysed by G.A. and A.F. supported by G.H.. G.H., J.W.H., G.A. and H.J. performed the simulations and G.H. devised the theory section. The study was planned and directed by C.R. and T.J.K. The manuscript was written by G.A., A.F., G.H., and C.R., after discussions with and input from all authors.

Additional information: Correspondence and requests for materials should be addressed to A.F., Y.Y., T.J.K. and C.R. (armin.feist@mpinat.mpg.de, yujia.yang@epfl.ch, tobias.kippenberg@epfl.ch, claus.ropers@mpinat.mpg.de)

Competing financial interests: The authors declare no competing financial interests.